Macromolecules

Article

Cite This: Macromolecules XXXX, XXX, XXX−XXX

# Molecular Simulation of Thermoplastic Polyurethanes under Large Tensile Deformation

Shuze Zhu,[†] Nikolaos Lempesis,[†] Pieter J. in 't Veld,[‡] and Gregory C. Rutledge*[,†]

[†]Department of Chemical Engineering, Massachusetts Institute of Technology, Cambridge, Massachusetts 02139, United States
[‡]BASF SE, ROM/AM, Carl Bosch Str, 38, 67056 Ludwigshafen, Germany

Supporting Information

**ABSTRACT:** Thermoplastic polyurethanes (TPUs) are useful materials for numerous applications due in part to their outstanding resilience and ability to dissipate energy under large mechanical deformation. However, the mechanistic understanding of the origins of these mechanical properties at the molecular level remains elusive, largely due to the complex, heterogeneous structure of these materials, which arises from the segregation of chemically distinct segments into hard and soft domains. In this work, molecular simulations are used to identify the mechanism of mechanical response under large tensile deformation of a common thermoplastic polyurethane comprising 4,4′-diphenylmethane diisocyanate and *n*-butanediol (hard segment) and poly(tetramethylene oxide) (soft segment), with atomic resolution. The simulation employs a lamellar stack model constructed using the Interphase Monte Carlo method established previously for semicrystalline polymers, which models the interfacial zone between hard and soft domains with thermodynamically rigorous distributions of bridges, loops, and tails. Molecular-level mechanisms responsible for yield, toughening, and the Mullins effect are reported. We have found several distinct mechanisms for yield and plastic flow, which we categorize as (i) cavitation, (ii) chain pull-out, (iii) localized melting with shear band formation, and (iv) block slip. The activity of these mechanisms depends on the topology of chains in the soft domain and the direction of loading (e.g., parallel or perpendicular to the interface). Further insights regarding toughening mechanisms and the Mullins effect are obtained from cyclic loading, where mechanisms ii to iv were found to be irreversible and account for the superior resilience and dissipation at large tensile strains in thermoplastic polyurethanes.

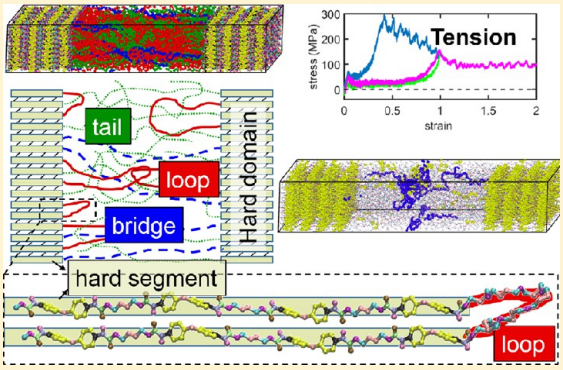


## 1. INTRODUCTION

Thermoplastic polyurethanes (TPUs) are linear, segmented block copolymers that have enjoyed growing commercial interest due to their remarkable versatility, mechanical properties, chemical properties, and wide spectrum of applications. Perhaps most remarkable are their outstanding toughness, durability, and ease of processing. They have found use in various demanding applications, including car instrument panels, autobody side molding, biomedical equipment, hydraulic hoses, sporting goods, high-performance films and sheet materials, medical tubing, adhesive coatings, and footwear.[1,2] More recently, they have found use as materials suitable for emerging manufacturing processes such as electrospinning,[3] additive manufacturing, and 3D printing.[4] Furthermore, they have been employed in applications such as biodegradable and biocompatible materials,[5] shape memory polymers,[6] self-repairing anticorrosion coatings,[7] superhydrophobic surfaces,[8] and lithium ion batteries.[9]

TPUs encompass an array of polyurethane plastics consisting of linear segmented, multiphase, heterogeneous block copolymers composed of hard and soft segments, which segregate on the nanometer length scale into hard and soft domains that are coupled mechanically through prolific interfacial zones. In such a picture, relatively ordered aggregates of the hard segments are interspersed at random orientations within an amorphous polymer matrix composed of soft segments. The hard domain is typically stiff and rigid, while the soft domain is typically compliant and flexible. A common type of hard segment is 4,4′-diphenylmethane diisocyanate (MDI) with *n*-butanediol (BDO) as chain extender[10] (henceforth denoted as MDI/BDO), while the soft segment is poly(tetramethylene oxide) (PTMO).[11]

Among the most impressive mechanical properties of TPUs are their outstanding resilience and dissipation under large strains. Slight changes in the fractions of hard and soft domains result in substantial changes in all of the elastic and inelastic features, including hysteresis and shape recovery. The remarkable combinations of elasticity and inelasticity are likely the result of interactions between spatially dispersed hard and soft domains in the materials, since performance and function are generally a consequence of structure. In fact, the mechanical behaviors have been extensively investigated for a broad range

Received: November 6, 2017
Revised: January 15, 2018




DOI: 10.1021/acs.macromol.7b02367
Macromolecules XXXX, XXX, XXX−XXX

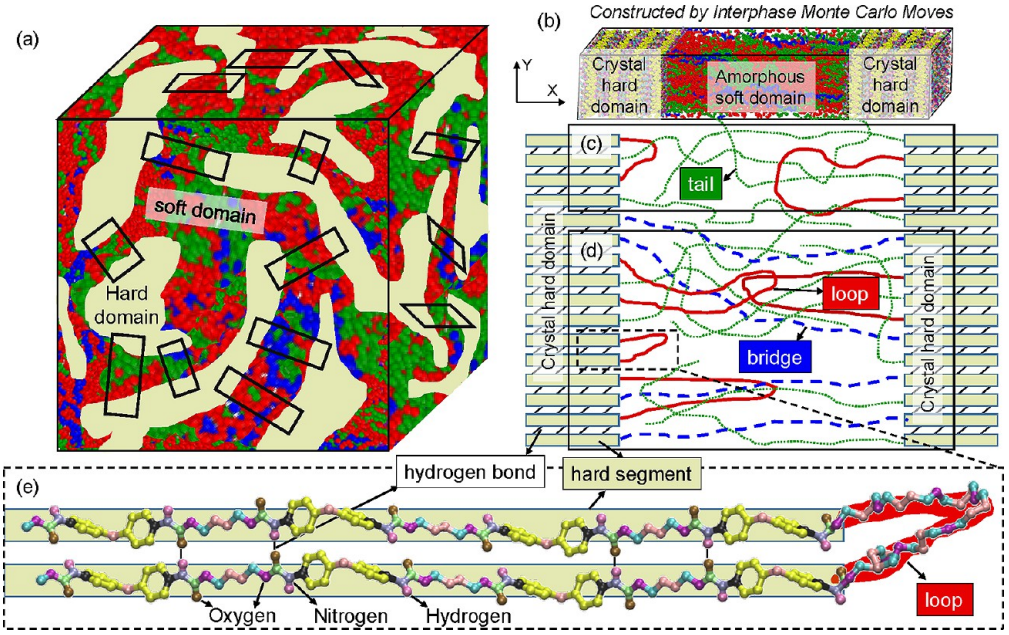


**Figure 1.** (a) Schematic showing a typical morphology of a TPU, where the hard domain is colored yellow, and the soft domain comprises bridge (blue), loop (red), and tail (green) segments; this color code is used throughout this report unless otherwise specified. Drawn throughout this schematic are smaller boxes comprising layers of hard and soft domains in approximately lamellar stacks. For purposes of this work, these lamellar stacks are the elementary building blocks, or representative volume elements (RVE), of the TPU morphology. Understanding the large strain deformation mechanisms of these lamellar stacks with atomistic resolution is the focus of this work. (b) A typical molecular configuration after Interphase Monte Carlo and molecular dynamics equilibration. (c) Schematic showing a system characterized topologically as "no bridges" for purposes of this work. In such systems, there are neither physical bridges nor bridging entanglements comprising crossed loops.[24,25] (d) Schematic showing a system characterized topologically as "with bridges" for purposes of this work. In such systems, there are physical bridges (blue dashed lines) or bridging entanglements comprising crossed loops. In this schematic, a single loop−loop bridging entanglement is shown. (e) The united-atom model for the chemical structure of hard segments and a loop soft segment. The atom types not labeled are carbon in united-atom representation. Note that the hydrogen bonding plane is parallel with the y direction in current work (Figure S2).

of polyurethanes and polyureas, where the two-phase features are found to play a critical role in the large deformation.[12−15] In the case of TPUs, it has been shown that the variations of the volume fractions and the intrinsic properties of the hard and soft constituents give rise to tunable resilient and dissipative mechanical responses at large strain.[16] However, the mechanistic understanding of the origins of the mechanical properties in this class of polymers under large strains at the molecular level remains elusive. For example, why are TPUs so tough?

To date, most numerical models to describe the deformation behavior of TPUs are on the macroscopic, continuum level. For example, Qi and Boyce used a continuum mechanics framework to model the large deformation behavior of TPUs in which a deformation-induced softening mechanism was introduced.[16] Often referred to as the "Mullins effect", such softening observed in the subsequent reloading cycles is an outstanding feature in this class of polymers, which leads to significant mechanical degradation and hysteresis upon deformation. However, the molecular origin of the Mullins effect in TPUs remains unclear. Qi and Boyce proposed a constitutive relation predicated on changes in mechanically effective volume fractions, which change as occluded soft domains become activated under deformation.[16] More recently, Cho et al. proposed a constitutive relation predicated on an irreversible breakdown of the hyperelastic network,[17] with comparable success. Experimentally, irreversible changes in the X-ray patterns during deformation indicate that microstructural breakdown in the hard domains is mainly responsible for softening and the related hysteretic behaviors of polyureas.[18] More recently, a combination of small- and wide-angle X-ray scattering (SAXS/WAXS) during cyclic tensile loading of a TPU in situ was used to elucidate the relationship between strains at different length scales, specifically atomic, nanoscale, and macroscale. In that work, the authors highlighted the importance of the "fuzzy interface" between the hard and soft regions, which they found to govern the structural evolution at nanometer length scales and lead to a reduction in macroscopic stiffness.[19] Nevertheless, the molecular mechanism operative in the "fuzzy interface" between hard and soft regions remains unknown.

Thus, despite numerous theoretical and experimental efforts, the physical picture for the atomistic origin of such softening, as well as hysteresis under large mechanical deformation, in this class of polymers remains unclear. As outlined above, one of the many intriguing missing pieces in this picture is the molecular mechanism of the microstructural breakdown in the hard domains in TPUs during large mechanical deformation. Furthermore, the analysis of the effect of chain topological types at the interface between soft and hard domains within this class of polymers on their mechanical behavior is important to understand and design these materials for various applications.

To gain insight into the fundamental molecular-level deformation mechanisms of a highly complex material system such as a TPU, one approach is to think of such a complicated structure as an aggregation of elementary building blocks comprising a hard domain, a soft domain, and the interface between them. By studying the more tractable problem of molecular deformation mechanisms within these elementary building blocks, one can begin to understand the processes operative throughout the complicated, heterogeneous morphol-


DOI: 10.1021/acs.macromol.7b02367
Macromolecules XXXX, XXX, XXX−XXX

ogy. In the case of a TPU, its complicated, heterogeneous morphology can be decomposed into an indefinite combination of many lamellar stacks, which are randomly oriented, as shown in Figure 1a. The investigation of the molecular deformation mechanism of these lamellar stacks is thus of fundamental significance. Nevertheless, no such large deformation study on lamellar stacks of TPU has been reported to date, largely due to the difficulty of constructing a reasonable model of the complex interphase topology.

In this work, we model the large tensile strain, plastic deformation of the elementary building blocks of a TPU (i.e., the lamellar stack) on a molecular level using atomistic Monte Carlo and molecular dynamics simulations. To our knowledge, this is the first such model of the large deformation mechanisms of a TPU. We examine in particular how the topology of loop and bridge segments within the soft domain affects the mechanism of large tensile deformation for a representative TPU. Using a Monte Carlo method originally developed for semicrystalline polymers, we construct a detailed, thermodynamically rigorous, atomistic model of the interfacial zone between hard and soft domains within TPUs, with thermodynamically consistent distributions of bridges, loops, and tails (Figure 1b). We deform these structures in tension using nonsteady state, nonequilibrium molecular dynamics simulations, identify the changes in structure that accompany mechanical loading, and correlate the molecular behavior to system observables like yield, toughening, and the Mullins effect. We have found several distinct mechanisms for yield, the importance of which depends on the topology of chains in the soft domain and the direction of loading. Further insights regarding toughening mechanisms and the Mullins effect are obtained from cyclic loading. Ultimately, we envision that the molecular mechanisms extracted from these simulations can be used to inform future multiscale approaches to modeling the complex but vitally important mechanical behaviors of multiphase heterogeneous polymers such as TPUs.

## 2. SYSTEM AND METHODS

To construct the model, we use the Interphase Monte Carlo (IMC) method of Rutledge and co-workers[11,20−25] as implemented in the EMC (Enhanced Monte Carlo)[22] software, version 9.3.7. Unless noted differently in this section, the force field, chemical composition, and model construction are identical to those used previously by Lempesis et al. to simulate the small strain, linear elastic response of TPUs.[26] These details are recapped below, but the reader is referred to the previous report for a more complete description. The TraPPE-UA (united atom) force field was used for the PTMO soft segments, but modified with harmonic bond stretching potentials. A force field based primarily on OPLS-UA, but modified with TraPPE-UA Lennard-Jones parameters, was used for the MDI/BDO hard segments. These force fields were previously validated on simulations of semicrystalline PTMO[11] and crystalline MDI/BDO.[10] The hard segments associate into hard domains, with hydrogen bonding represented implicitly through a combination of Coulombic and Lennard-Jones interactions. Auxiliary calculations of energy versus separation distance between two hard segments indicated an effective hydrogen bonding energy of 14.98 kJ/mol (Figure S1), which agrees quite well with the hydrogen bonding energy from first-principles calculations,[27,28] further confirming the validity of the force field. It is critical to note that in the models of current study hydrogen bonds between segments in the hard domain occur within planes that are parallel with the $y$-direction.

Atomistic configurations of TPUs were created using the IMC method as if the heterogeneous TPUs were semicrystalline polymers, having a crystalline MDI/BDO layer and an amorphous PTMO layer. In general, the model created by the IMC method is a one-dimensional lamellar stack that consists of noncrystalline domains sandwiched between crystalline domains, as shown in Figure 1 (see also Figure S2). Initially, a triclinic crystalline simulation cell containing $10 \times 10 \times 9$ ($N_a \times N_b \times N_c$, where $N_i$ is the number of MDI/BDO unit cells along the $i$-direction, $i = a, b, c$) MDI/BDO unit cells was constructed, and a layer 5 unit cells thick (in the $c$-direction) was removed and replaced by PTMO chain segments having three repeat units per MDI/BDO repeat unit; chemical bonding between MDI/BDO and PTMO segments was enforced at each interface (Figure S2). In this work, the $c$-direction is oriented along the $x$-axis, and the MDI/BDO structural units are chemically bonded across the periodic boundary in the $x$-direction. Then, 25−95 of the PTMO segments were cut, and 700−1200 UA sites were removed from these PTMO segments, resulting in a reduced density of about or below 1.0 g/mL in the PTMO layer, which evolves to an amorphous phase upon equilibration during IMC simulation. Chain end sites were introduced to terminate the cut PTMO soft segments and to facilitate Monte Carlo sampling. The sizes of the hard and soft domains in the $x$-direction are based on X-ray diffraction data, which indicate a typical hard domain thickness of four MDI/BDO repeat units,[29−34] and compositional information, which dictates the volume fractions of hard and soft domains (or their thicknesses). Variation of the number of cut segments and removed UA sites as described above resulted in a significant variation of interphase topology in the structures created by the IMC method. The composition also varied, but the mass fraction of hard domain in the TPU remained roughly around 55 ± 2%, in accordance with a composition that has been characterized experimentally.[17] In the y- and z-directions, the simulation size is mainly limited by the computational complexity of such models with atomistic resolution, on the order of 35 000 sites. Taken together, the alternating layers of soft and hard domains comprise a "lamellar stack" motif, which we envision as the most basic building block of the TPU morphology.

Monte Carlo moves were employed that displace atoms and alter the polymer chain connectivity through cutting and splicing, in order to sample new configurations and topologies within the PTMO domain. Topology is characterized by the set of loops, bridges, and tails within the PTMO soft domain. "Bridges" span the soft domain and connect two hard domains through an intramolecular linkage, "loops" connect two points in the same hard domain, and "tails" terminate somewhere in the soft domain. Both hard and soft domain layers are semi-infinite due to periodic boundary conditions in the lateral directions and the lamellar stack repeats due to periodic boundary conditions in the stack direction. Chain connectivity between hard and soft segments was maintained throughout the simulation. More details about the chemical structure of TPUs, the model used in this study, and the procedure used to generate such a model are further illustrated in Figure S2.

A set of 15 TPU configurations was generated by unbiased sampling from the equilibrium distribution of topologies created by the IMC method. These configurations were then analyzed to quantify their topological features[25] and categorized according to topology as depicted in Figure 1, which shows the crystalline lamellae (hard domain) and the amorphous layer (soft domain), with loops, bridges, and tails. Although each configuration differs in the numbers, lengths, and conformations of bridges, loops, and tails, we found it sufficient for purposes of mechanical characterization to apportion all of the configurations into one of two types of system topologies: "with bridges", represented by Figure 1d, having at least one bridge segment or bridging entanglement[24,25] between loops emanating from opposite interfaces, and "no bridges", represented by Figure 1c, having neither of these topological entities. We report the result of one such set of configurations in this work, the features of which are listed in Table 1.

The configurations of TPUs generated by IMC were imported to LAMMPS[35] for subsequent molecular dynamics analysis. Prior to nonequilibrium molecular dynamics simulation of large mechanical deformation, all configurations were equilibrated for at least 2 ns by molecular dynamics simulations in the $N\sigma T$ statistical ensemble at $T$ = 300 K until all normal stress components were equal to about 1 atm, all shear stress components were close to zero, and the density of the


DOI: 10.1021/acs.macromol.7b02367
Macromolecules XXXX, XXX, XXX−XXX

**Table 1. Configurations of TPUs Studied in This Work**

| system topological category | configuration no. | no. of bridges | no. of loops | no. of loop−loop bridging entanglements | no. of tails |
|---|---|---|---|---|---|
| no bridges | 1 | 0 | 75 | 0 | 50 |
| no bridges | 2 | 0 | 25 | 0 | 150 |
| no bridges | 3 | 0 | 5 | 0 | 190 |
| no bridges | 4 | 0 | 43 | 0 | 114 |
| no bridges | 5 | 0 | 37 | 0 | 126 |
| with bridges | 6 | 8 | 52 | 0 | 80 |
| with bridges | 7 | 15 | 48 | 0 | 74 |
| with bridges | 8 | 6 | 39 | 0 | 110 |
| with bridges | 9 | 10 | 24 | 0 | 132 |
| with bridges | 10 | 0 | 59 | 1 | 82 |
| with bridges | 11 | 0 | 45 | 1 | 110 |
| with bridges | 12 | 0 | 44 | 2 | 112 |
| with bridges | 13 | 5 | 58 | 1 | 74 |
| with bridges | 14 | 14 | 47 | 2 | 78 |
| with bridges | 15 | 10 | 58 | 2 | 64 |

system was converged. $N$ denotes total number of UA sites, $\sigma$ is stress, and $T$ is temperature. Temperature and stress were maintained using the Nosé−Hoover thermostat and barostat (temperature damping parameter was 50 time steps and stress damping parameter was 500 time steps), respectively. The time step was 2 fs. Explicit evaluation of Lennard-Jones and Coulombic interactions was truncated at a cutoff distance of 0.95 nm, while the evaluation of long-range Coulombic interactions at larger separation distances was done in reciprocal space. The final simulation box was triclinic as a result of the original triclinic MDI/BDO crystal structure and the subsequent equilibration in the $N\sigma T$ ensemble.

After equilibration, deformation was applied using nonequilibrium molecular dynamics simulation in which one dimension of the simulation box was incremented at each step of the simulation to produce constant strain rate deformation in an $N\varepsilon T$ ensemble for tensile deformation as explained below. The temperature was maintained at 300 K. In the current study, the maximum engineering tensile strain was 200%. Three orthogonal loading directions ($x$, $y$, and $z$) were considered, and the "simple strain" deformation protocol was applied. The lamellar stack was deformed with only one component of the strain tensor nonzero at a constant engineering strain rate. We employed this simple strain deformation protocol in an attempt to project the deformation mechanisms onto each individual normal strain component, which we believe provides the most direct insight into deformation response. Experimentally, a uniaxial deformation, in which strain components other than the one being driven are allowed to vary in order to maintain a constant (usually zero) stress, is more common. The two modes of deformation are related; uniaxial tension may be viewed as a combination of simple tensions or compressions along three different axes, and we have previously[10,11,26] shown that either method leads to consistent determinations of elastic moduli, for example. Of greater importance to this work, the underlying mechanisms of response, occurring either individually or in combination, are expected to be the same. The time step was 2 fs, and the engineering strain rate was $5 \times 10^7$ s$^{-1}$. The high strain rate used in this work is typical of molecular dynamics simulations and is always a source of some concern. Even the simulated elastic constants for these TPUs have been found to be rate-dependent, as shown previously by Lempesis et al.[26] Nevertheless, in many simpler polymer systems, both amorphous and crystalline molecular dynamics simulations have been found to reproduce, at least qualitatively, many of the important features of stress versus strain observed experimentally. The instantaneous stress tensor components of the system were computed according to the method proposed by Irving and Kirkwood.[36] Time averages of the six stress tensor components were taken at frequent time intervals during the entire simulation. Engineering stress−strain curves are reported in the current study. Unless noted otherwise, the stress reported is the normal stress component along the loading direction. For cyclic loading, the unloading stops when the stress is at or about to cross zero. All simulations were re-equilibrated using molecular dynamics simulations

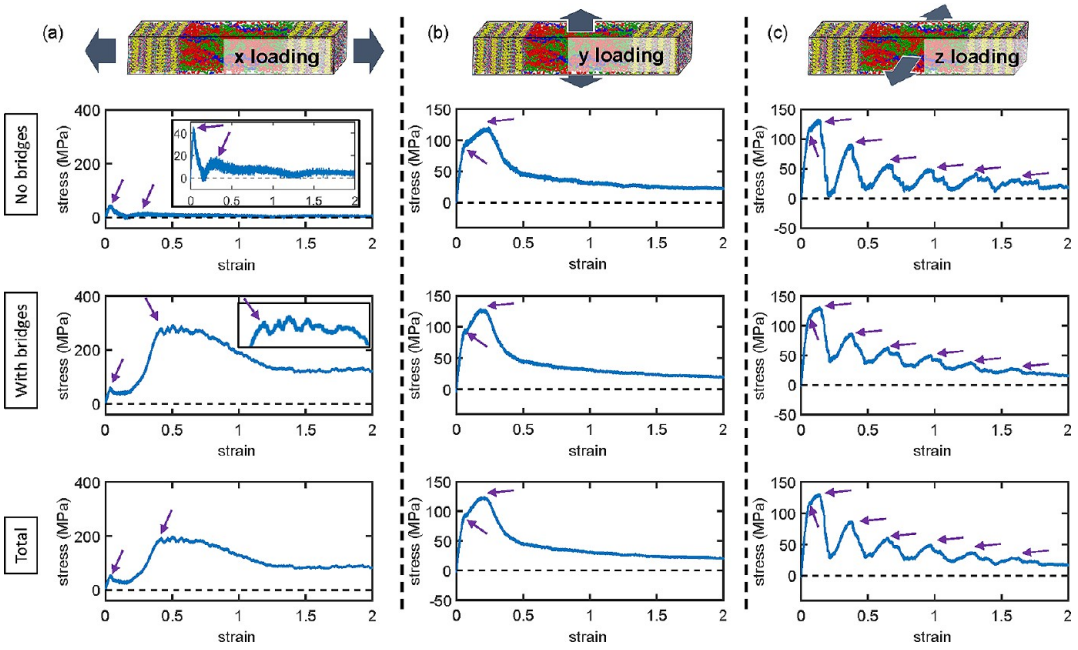


**Figure 2.** Engineering stress−strain curves in tensile deformation, averaged over "no bridges" configurations only (first row), "with bridges" configurations only (second row), and all configurations (third row). The stress reported here is the normal stress component along the loading direction. Columns separated by dashed lines denote corresponding loading directions ($x$, $y$, and $z$), which are orthogonal to each other. Note that the stress scale under $x$-loading is more than 2 times larger than that for $y$- or $z$-loading. Purple arrows on stress−strain curves point to salient yield events. Refer to Figure S3 for other components of the stress tensor orthogonal to the loading directions. Refer to section 3.1 for a summary of these mechanical responses and section 3.2 for detailed mechanisms to account for these responses.



DOI: 10.1021/acs.macromol.7b02367
Macromolecules XXXX, XXX, XXX−XXX

in the $N\sigma T$ statistical ensemble at $T$ = 300 K and $P$ = 1 atm between the first unloading and the second loading.

Figure 1e shows the UA model for the chemical structure of two hard segments on one side of the periodical boundary connected by a soft "loop"-type segment. The hard segments associate into hard domains via hydrogen bonding. The hydrogen bonds between segments in the hard domain occur within planes that are parallel to the $y$-direction (Figure S2). Figure 1b presents a typical molecular model after equilibration by IMC and molecular dynamics simulations. The PTMO segments within the soft domain are colored-coded throughout this report (cf. Figure 1 caption for details) unless otherwise specified.

## 3. RESULTS AND DISCUSSION

**3.1. Stress−Strain Behavior in Tension to Large Deformation.** Figure 2 shows the ensemble-averaged stress−strain curves in $x$, $y$, and $z$ directions for tensile deformation of the simulation cell. Results are shown for the "no bridges" and "with bridges" subensembles as well as for the total ensemble of 15 configurations in Table 1. First, we note that different directions of loading lead to very different stress−strain curves. Such observations suggest that the microscopic mechanism of large strain in deformation of TPUs is highly complex and anisotropic on the domain length scale. In the lamellar stack model, at the simplest level of interpretation, deformation along the $x$-direction loads both hard and soft domains in series, analogous to a Maxwell model where mechanical elements experience similar stresses but their strains are different, while deformation along the $y$- and $z$-directions loads the hard and soft domains in parallel, analogous to a Voigt model where mechanical elements experience the same strain but their stresses are different. The role of the hard domain is more apparent in the $y$- and $z$-strain cases. The responses in $y$- and $z$-directions are similar, since both are analogous to a Voigt model, but not equivalent. The difference here lies in the orientation of the hydrogen bonded planes in the hard domain, which respond differently when strain occurs parallel or perpendicular to the hydrogen bonds.

When we look at the stress−strain curves in more detail, for tensile straining along the $x$- (stack) direction, the total ensemble averaged stress−strain curve in Figure 2a shows two yield events. The first yield event happens around a strain of 5%, with a yield stress around 50 MPa. The second yield happens around a strain of 40%, with a yield stress around 200 MPa. It is worth noting that strain and stress for the first yield event are almost the same in all three ensembles, which suggests that the deformation mechanism for tensile straining along the $x$-direction up to the first yield is independent of the system topology. By contrast, the mechanical behavior for the second yield event differs among the three ensembles. The "no bridges" subensemble displays a much lower stress level after the first yield event, with a yield stress around 15 MPa at 30% strain, while the "with bridges" subensemble exhibits a much higher stress level after the first yield event, with a yield stress around 280 MPa at 40% strain. Also, the "with bridges" subensemble displays a series of tiny "sawtooth" features in the stress−strain response. These observations suggest that the deformation mechanism for tensile straining along the $x$-direction after the first yield is dependent on the system topology.

For tensile loading in the $y$- and $z$- (both lateral) directions, the mechanical responses are qualitatively similar for all three ensembles, regardless of system topology. Tensile straining along the $y$- (first lateral) direction again shows two yield events (Figure 2b). In the total ensemble, the first yield event happens around a strain of 5%, with a yield stress around 90 MPa, and the second yield event happens around a strain of 20%, with a yield stress around 125 MPa. In addition, hardening is observed after the first yield event until the second yield event, since the stress increases in this range; this observation is another important difference from Figure 2a. Tensile straining along the $z$- (second lateral) direction shows multiple yield events, as indicated by the sawtooth features in Figure 2c. The first yield event happens around a strain of 5%, with a yield stress around 120 MPa, followed by the second yield event around a strain of 15%, with a yield stress around 130 MPa. We also see hardening between the first and second yield events, similar to tensile strain along $y$ shown in Figure 2b. Subsequent cycles of softening and hardening are observed in each ensemble, with decaying yield stress as strain increases. Interestingly, we observe that the amount of relaxation in stress for the "with bridges" subensemble is much less than that for the "no bridges" subensemble. Although the yield stresses are quantitatively similar (e.g., the first yield stress around 120 MPa, the second around 130 MPa, and the third around 80 MPa) for both "with bridges" and "no bridges" subensembles, the ensuing local minima in stress of the "with bridges" subensemble are much higher than those of the "no bridges" subensemble. The amount of stress drop is mitigated in the "with bridges" subensemble. Such observation indicates some difference in the deformation mechanism for the "with bridges" ensemble when strained along the $z$-direction.

**3.2. Molecular Interpretation of Stress−Strain Response in Tensile Deformation.** Molecular simulation allows one to examine the molecular rearrangements that take place upon deformation, with atomic resolution. By so doing, one can identify the mechanisms responsible for the observed stress−strain responses exhibited in Figure 2. Upon close inspection of the stress−strain curves and the structural evolution of hard and soft domains during loading for each configuration in the ensemble, we are able to identify several distinct deformation mechanisms in accordance with aforementioned observations and analysis for ensemble averaged stress−strain curves.

In anticipation of the following discussion, we define four such mechanisns: cavitation, chain pull-out, melting, and block slip. "Cavitation" refers to the formation of regions of localized low (or zero) density. These regions apparently nucleate under dilatational stresses and grow in size as the strain progresses. "Chain pull-out" refers to the extraction of a hard segment from the hard domain to the soft domain under an applied stress. "Melting" refers to locally disordered regions in the crystalline hard domain where the hard segment conformations and packing deviate significantly from the crystallographic form. "Block slip" refers to shear events in the hard domain wherein displacement is localized between groups of hydrogen-bonded planes, or 'blocks"; this mechanism may be constrasted with "fine slip", wherein shear would be more uniformly distributed over the entire hard domain. The deformation mechanisms tend to be dependent on the system topological category and loading direction and therefore are discussed in greater detail using several configurations as illustrations. Since it is not practical to present all 15 configurations, the selected configurations are intended as representative of the whole ensemble to illustrate and explain the mechanism. In fact, we have visually inspected all of the configurations and confirmed that the highlighted behavior holds for all configurations within


DOI: 10.1021/acs.macromol.7b02367
Macromolecules XXXX, XXX, XXX−XXX

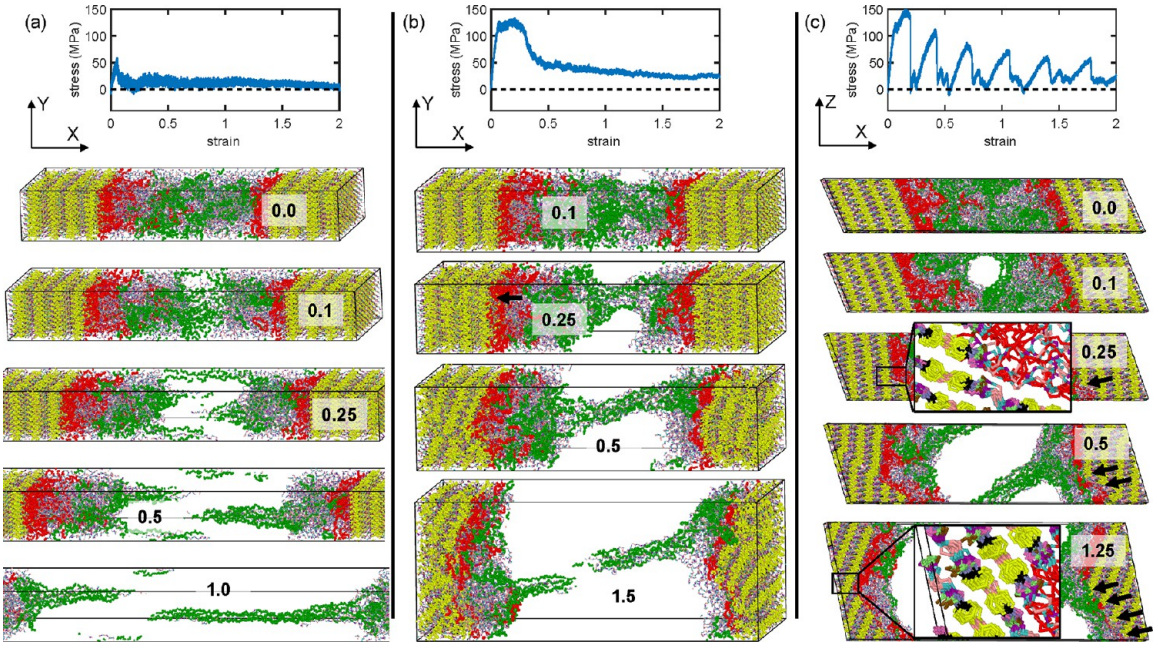


**Figure 3.** Engineering stress−strain curves and structural evolutions of configuration 1 ("no bridges") during tensile straining along (a) *x*-, (b) *y*-, and (c) *z*-directions. The stress reported here is the normal stress component along the loading direction. For each loading direction, snapshots of the configuration are shown and labeled with the strain; viewing perspectives along *z* or *y* are indicated by the coordinate axes, in black. In the soft domain, all "loops" are colored red. Only the "tails" that are still entangled and "bridging" two hard domains at strain 1.0 during tensile straining along *x*-directions are colored green. The remaining tails are colored by atom types (Figure 1e). In (a), cavitation in the soft domain is observed. In (b), the black arrow at 25% strain points to a locally disordered region in the crystalline hard domain that later develops into melting. In (c), the black arrows point to locations where new surface has been created by block slip in the hard domain. Each arrow points to the stacked array of aromatic carbon rings on such a surface. The two insets at 25% and 125% strains in the third column are magnifications of a part of the hard domain to show the molecular structure near such a surface. The number of arrows for each structure at a particular strain equals the number of drastic stress drop events occurring up to this level of strain. The sharp contrast between the two lateral loadings is related to the orientation of hydrogen bonding plane (Figure S2), and it is found universally applicable. Cavitation, melting, and block slip in the hard domain also apply to the "with bridges" ensemble.

an ensemble. The core message conveyed by this work is the large tensile deformation mechanisms governing yield and toughening.

Essentially, we want to answer six questions for the tensile deformation mechanism. Question 1: why is the mechanical response direction-dependent? Question 2: why do both subensembles exhibit the same first yield event when strained in the *x*-direction? Question 3: why does the "with bridges" subensemble exhibit a much higher stress level than the "no bridges" subensemble after the first yield event when strained in the *x*-direction? Question 4: why do both subensembles exhibit the same yield events, when strained in the *y*-direction? Question 5: why do both subensembles exhibit multiple yield events when strained in the *z*-direction? Question 6: why is the amount of relaxation in stress for the "with bridges" subensemble much less than that for "no bridges" subensemble when strained in the *z*-direction?

Figure 3 serves to answer questions 1, 2, 4, and 5. Here, we present the molecular mechanisms that underlie the observed mechanical response in tension for a typical configuration from the "no bridges" subensemble; the mechanism described is generally applicable to the whole ensemble. Clearly, there are huge differences between the structural evolutions for the three loading directions. When the entire simulation cell is strained along the *x*- (stack) direction, the same amount of stress is borne by the soft and hard domains individually due to their being in mechanical equilibrium, analogous to mechanical resistances in series. Given the huge difference between the mechanical stiffnesses of soft and hard domains, most of the strain occurs within the soft domain, while the hard domain remains essentially intact. Therefore, the stress−strain curve in Figure 3a carries more information about the deformation of soft domain than hard domain. Examination of the snapshots in Figure 3a indicates that the first yield event, occurring around 5% strain, can be attributed to cavitation in the soft domain, which is already significant by 10% strain. Cavitation occurs at small strain because moderate dilatational stresses build up quickly with tensile deformation when the lateral dimensions are fixed, as was the case for the simple strain deformations employed here. The normal stresses orthogonal to the loading directions were also calculated; their ensemble-averaged values are reported in the Supporting Information (Figure S3). However, these other stresses are usually much smaller in magnitude than the normal stress along the loading direction and so are not reported here in detail. Importantly, these stresses tend to be dilatational. Thus, the cavitation that occurs at small strains is a consequence of the deformation mode employed. When the elastic energy exceeds the energy required to form a new surface, formation of a cavity is energetically preferred. Such cavities form more readily in the soft domain than in the hard domain. The subsequent stress drop occurs as the cavity rapidly expands. Once the cavity approaches the dimension of the simulation cell, the stress increases again due to the stretching among entangled tails and loops (e.g., see structure at strain of 25%). The second yield event is then attributed to the unravelling and sliding of these entangled tails


DOI: 10.1021/acs.macromol.7b02367
*Macromolecules* XXXX, XXX, XXX−XXX

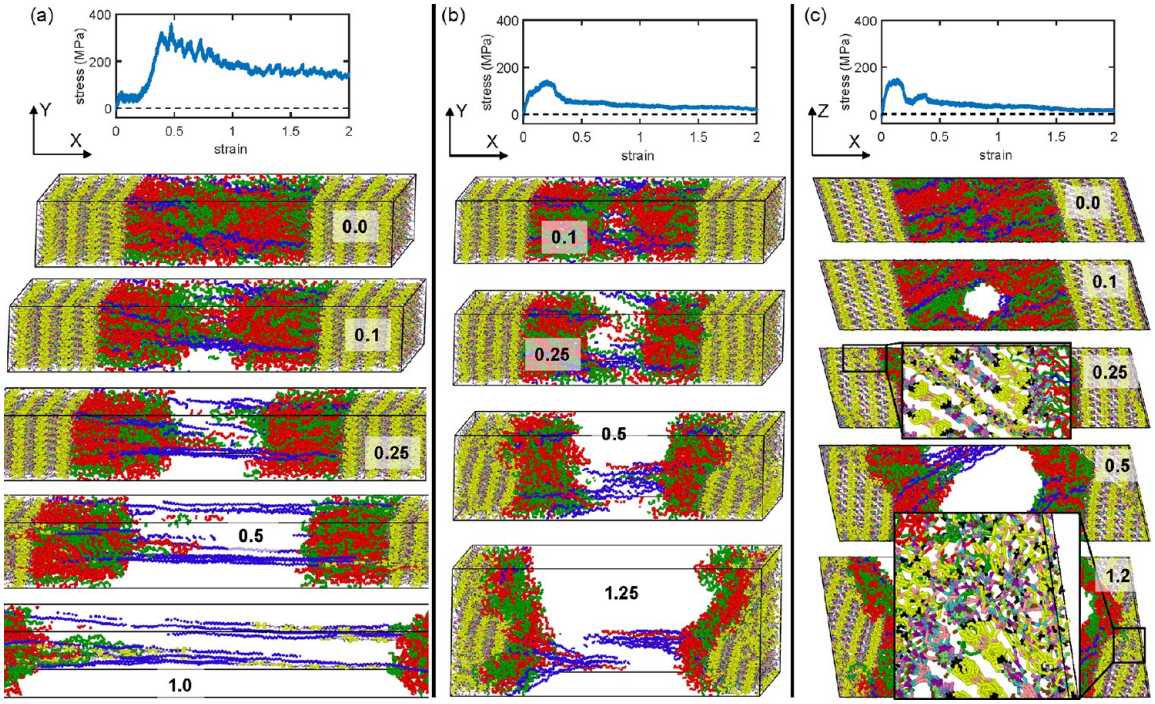


**Figure 4.** Engineering stress−strain curves and structural evolutions of configuration 6 ("with bridges") during tensile straining along *x* (a), *y* (b), and *z* (c) directions. The stress reported here is the normal stress component along the loading direction. For each loading direction, snapshots of the configuration are shown and labeled with the strain; viewing perspectives along *z* or *y* are indicated by the coordinate axes, in black. In the soft domain, all "loops" are colored red, all "bridges" are colored blue, and all "tails" are colored green. In (a), hard segments are pulled out from crystal domain. In (b), a locally disordered region emerges in the crystalline hard domain after 25% strain. In (c), block slip is observed in the hard domain as strain increases. The insets in (c) at 25% and 120% strain are just magnified views of a part of the model to show emerging disordered regions between two blocks near the new surface created by block slip. The bridges are also straightened as block slip continues. The disordered regions and the bridging constraints both prevent the drastic drop in stress observed with block slip in the "no bridges" subensemble, which therefore mitigates the stress relaxation.

and loops under stress, followed by plastic flow. As one can see from the structural evolution up to a strain of 100%, tails become straightened and slide past one another. There are almost no other types of polymer chains bridging the soft domain at 100% strain than those tails colored in green. Thus, the entangled long tails are load-carrying (i.e., "entangled") initially but creep at constant stress until they ultimately separate completely. In the case of configuration 1, long-range plastic flow has been observed after the second yield event since there are still entangled tails even at very large strain; around 200% strain, the stress drops to zero, indicative of complete fracture. The range of such plastic flow varies for other configurations in the ensemble of "no bridges".

When strained along the *y*- or *z*- (lateral) directions, the soft and hard domains strain equally, analogous to mechanical resistances in parallel. Since the hard domain is much stiffer than the soft domain, the majority of stress is carried by the hard domain in these cases, and therefore the maximum stress level is much larger than that experienced upon deformation in the *x*-direction. When deformed in the *y*-direction, the structural evolution of the soft domain indicates that the first yield event is associated with cavitation in the soft domain. The cavity can be readily seen in the structure at 10% strain in Figure 3b. After the cavitation in the soft domain, almost all of the stress is then carried by the hard domain. Therefore, the continuous increase in stress until the second yield event is caused by the stretching of the hard domain until its crystal structure can no longer be maintained (at the second yield strain). Locally disordered regions start to appear, and stress begins to drop after the second yield strain. We can see some locally disordered regions in the crystalline hard domain in the structure at 25% strain in Figure 3b. The further emerging of locally disordered regions gives rise to a melting-like behavior (see structures at 50% strain and at 150% strain in Figure 3b; also see Figure S4) on a larger scale in the hard domain, accompanied by a significant drop in stress. The plastic flow in the stress−strain curve after the second yield event is mainly caused by deformation and flow as the hard domain melts (i.e., locally disordered regions within the hard domain grow), since the system obtains a much higher plastic flow stress (e.g., around 25 MPa) than that typical of deformation in the soft domain, as shown in Figure 3a.

When deformed in the *z*-direction, the structural evolution of the soft domain suggests that the deformation mechanism before the stress drop is the same as that in the *y*-direction. However, unlike Figure 3b, instead of locally disordered regions, block slip events start to appear, and stress begins to drop drastically after the second yield strain. The stress decreases as the block slip takes place until the resultant configuration is stabilized. As evidence of this behavior, the magnified insets in Figure 3c show nicely restacked arrays of aromatic carbon rings, corresponding to a state of local stress minimum. The initiation of the second and subsequent block slip events can be understood as follows: the deformation increases the strain energy of the current configuration until enough strain energy is accumulated to overcome the energy barrier for the next block slip event to occur. Such a process repeats itself during further loading, as indicated by the


DOI: 10.1021/acs.macromol.7b02367
*Macromolecules* XXXX, XXX, XXX−XXX

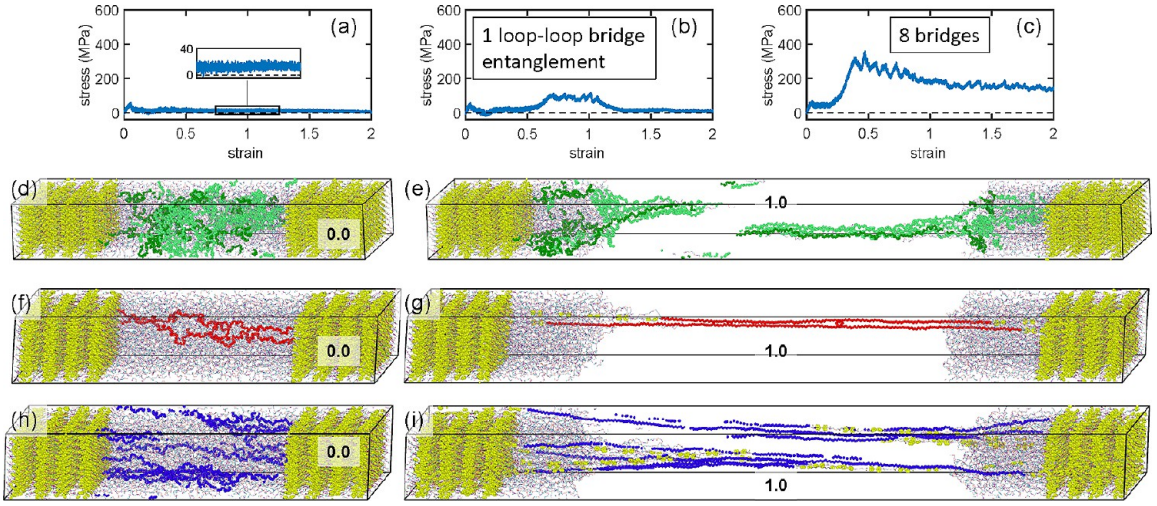


**Figure 5.** Engineering stress–strain curves and structural evolutions during tensile straining along *x*-directions, showing the effect of bridges and bridging entanglements, for several configurations. The stress reported here is the normal stress component along the loading direction. Configuration 1: (a, d, e), 0 bridges; configuration 11: (b, f, g), 1 loop–loop bridging entanglement (colored in red); configuration 6: (c, h, i), 8 bridges (colored in blue). In (d) and (e), two different shades of green are used to distinguish entangled tails originating from the left interface (dark green) from those originating from the right interface (light green). It is found that the strength is approximately linearly proportional to the number of hard segments pulled out. See more discussion in the main text and Figure S8.

sawtooth features of the stress–strain curve. More evidence for the structural evolution in this case can be found in Figure S5. The detailed process of initiation and completion of block slip is shown in Figure S6. From the molecular structure near the slip plane (e.g., magnified insets in Figure 3c, Figure S5, and Figure S6), we find that the state where the stress is in a local minimum usually shows good stacking between the aromatic carbon rings. This explains the appearance of discrete intervals of equal strain between these slip events, which reflects the stacking periodicity of the aromatic carbon rings.

Although the tensile loadings along the *y*- and *z*-directions both involve pulling the lamellar stack in a lateral direction, we observed very different mechanical responses in these two directions. This is largely due to the orientation of hydrogen bonds in the hard domains, which lie more closely parallel with the *xy*-plane, giving rise to planes of hydrogen-bonded hard segments. Thus, tension along *y*-direction loads the hydrogen bonds themselves, while tension along the *z*-direction loads the weaker van der Waals interactions between hydrogen-bonded planes (see Figures S1, S2, and S4–S6). Therefore, tensile deformation along the *z*-direction is energetically favorable for block slip in the hard domain, which needs only overcome steric interactions, while tensile deformation along the *y*-direction involves the disruption of hydrogen bonds within planes, resulting in the melting-like behavior in the hard domain and reconfiguration of the hydrogen bonding network into a more amorphous configuration. The events of breaking and re-forming of hydrogen bonds typically do not happen simultaneously in the hard domain; therefore, there is no characteristic pattern (i.e., zigzag feature) in the stress–strain curves. Nevertheless, if one compares the areas beneath the stress–strain curves in Figures 3b and 3c, which represent the mechanical work done on the material in each case, one can see that the total energy dissipated by block slip is also large, comparable to that associated with disruption of hydrogen bonds. Such observation is also true for the ensemble-averaged stress–strain curves in Figure 2. Thus, both mechanisms of hydrogen bond disurpton and block slip are dissipative and significant sources of toughness.

The foregoing discussion of configuration 1 sheds light on the mechanisms of response to tensile deformation in the absence of bridges or bridging entanglements. When further examining the deformation mechanisms in the "with bridges" subensemble, we find that many characteristics of the deformation mechanisms identified in the "no bridges" subensemble are still valid and in effect. When strained along the *x*-direction, the first yield event is associated with cavitation. When strained along the *y*-direction, the stress drop is associated with melting in the hard domain. When strained along the *z*-direction, the sawtooth feature in the stress–strain curve is due to the block slip in the hard domain. These same mechanisms are apparent in Figure 2, where similar features, and the corresponding mechanism, arise. However, there are some observations in the stress–strain curve of the "with bridges" subensemble that are qualitatively and quantitatively different than that of the "no bridges" subensemble. Specifically, we can address questions 3 and 6. We find that the answers to these questions reveal new mechanisms associated with the role of bridges and bridging entanglements in the soft domain.

To address questions 3 and 6, Figure 4 shows a configuration from the "with bridges" subensemble, emphasizing the new mechanisms associated with the effects of bridging in the soft domain. Clearly, there are significant differences between the structural evolutions for the three loading directions. For tensile deformation along the *x*-direction at small strain, the deformation mechanism is the same as that of the "no bridges" subensemble (Figure 3a). However, the stress quickly increases until the second yield event. The mechanism for the stress increase before the second yield event, as established for the ensemble of "no bridges" in Figure 3, now becomes apparent: the subsequent huge increase in stress is mainly due to the straightening and stretching of bridges rather than entangled tails. However, instead of untangling, these bridges accumulate strain energy up to a critical point, at which the bridges begin to pull the hard segments to which they are connected out of the hard domain, as shown in the structure at 50% strain. The onset of this pulling out of hard segments signifies the second yield event. The salient sawtooth features after the second yield event


DOI: 10.1021/acs.macromol.7b02367
*Macromolecules* XXXX, XXX, XXX–XXX

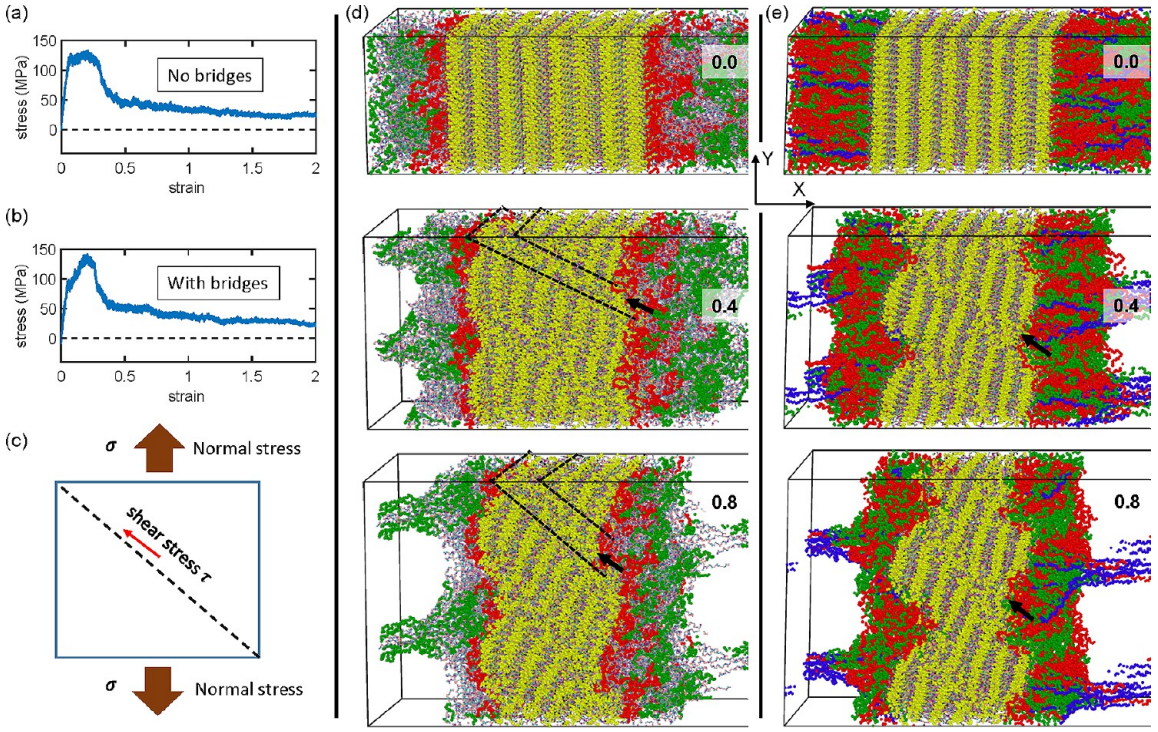


**Figure 6.** Engineering stress−strain curves and evolution of structure, showing formation of shear bands in the hard domain during lateral tensile straining along the *y*-direction. The stress reported here is the normal stress component along the loading direction. Configuration 1: (a, d) the color code is the same as in Figure 3; configuration 6: (b, e) the color code is the same as in Figure 4. The activation of shear stress during tension from a mechanical perspective is depicted in (c). The arrows in the configuration snapshots point to the location of the shear bands. Strain values are labeled on each snapshot. Each snapshot shows two periodic images of the simulation cell, translated along the *x*-direction to put the hard domain at the center. It is found that when straining laterally parallel with the hydrogen bonding plane, shear stress causes melting behavior in the hard domain. Please note that the hydrogen bonding plane is parallel with the *y*-direction (Figure S2).

indicate that the continued pulling out of hard segments is periodic and repetitive, analogous to the block slip events. The pulling out of a single hard segment requires the accumulation of strain energy, which manifests as the increase in stress, and this stress then drops as the hard segment translates by one repeat unit. The detailed process of pulling out of hard segments is shown in Figure S7. Such a process could repeat itself upon further loading so that more hard segments are successively pulled out, as seen in the structure at 100% strain. The pulling out processes may not happen simultaneously. Collectively, such processes render the sawtooth feature in a stress−strain curve. At the molecular level, such pulling out processes involve the breaking and re-forming of hydrogen bonds between hard segments and the restacking of aromatic carbon rings.

For tensile deformation along the *y*-direction (Figure 4b), the deformation mechanism is the same as that for the "no bridges" subensemble (Figure 3b). However, for tensile straining along the *z*-direction, even though we observe the block slip behavior within the configuration, the stress−strain curve does not exhibit the characteristic sawtooth behavior. From the molecular structure near the slip surface (e.g., see the magnified insets in Figure 4c), we find locally disordered regions, as indicated by the disordering of the stacking between aromatic carbon rings. We also find that the bridges are gradually straightened as the strain increases, which can be seen in the configuration at 50% strain in Figure 4c. Similar to the disordered and melting regions seen in Figures 4b and 3b, the existence of disordered regions in Figure 4c, which later develop into melting regions in the hard domain as strain increases, prevents the sharp drop in stress. We conclude that the gradually straightened bridges impose constraints on the motion of hard segments during block slip, which have the effect of restraining the block slip motion and preventing sharp drops in stress. These stretched bridges can also release some amount of the strain energy during block slip, which may also serve to offset any sharp drop in stress associated with block slip. Further mechanistic understandings on the emerging of disordered and melting regions, and the correlation between disordered regions, bridging effects, and stress relaxation, when the lamellar stack is strained along lateral direction, are discussed later in the context of Figures 6 and 7.

Figure 5 illustrates the effect of bridges and loop−loop bridging entanglements on the mechanical properties of the lamellar stack when strained along the *x*-direction. It is clear that both the strength (i.e., the maximum stress) and toughness (i.e., the area beneath the stress−strain curve) increase as the number of bridges or loop−loop bridging entanglements increases (from Figure 5a to 5c). In the absence of bridges or loop−loop bridging entanglements (Figure 5a), the strength relies primarily on the resistance to disengagement of tail−tail or tail−loop entanglements. The plastic flow (e.g., the inset in Figure 5a) originates from the unravelling and sliding of entangled tails and loops until completely disentangled. Figures 5d and 5e illustrate the straightening and sliding of entangled tails, as evidenced by tails originated from either the left or right interface spanning the cavitation zone. Bridges and loop−loop bridging entanglements, by contrast, can only be extended until taut, as which point the high level of stress involved triggers the pulling out of hard segments (e.g., Figure 5g,i). For cases


DOI: 10.1021/acs.macromol.7b02367
*Macromolecules* XXXX, XXX, XXX−XXX

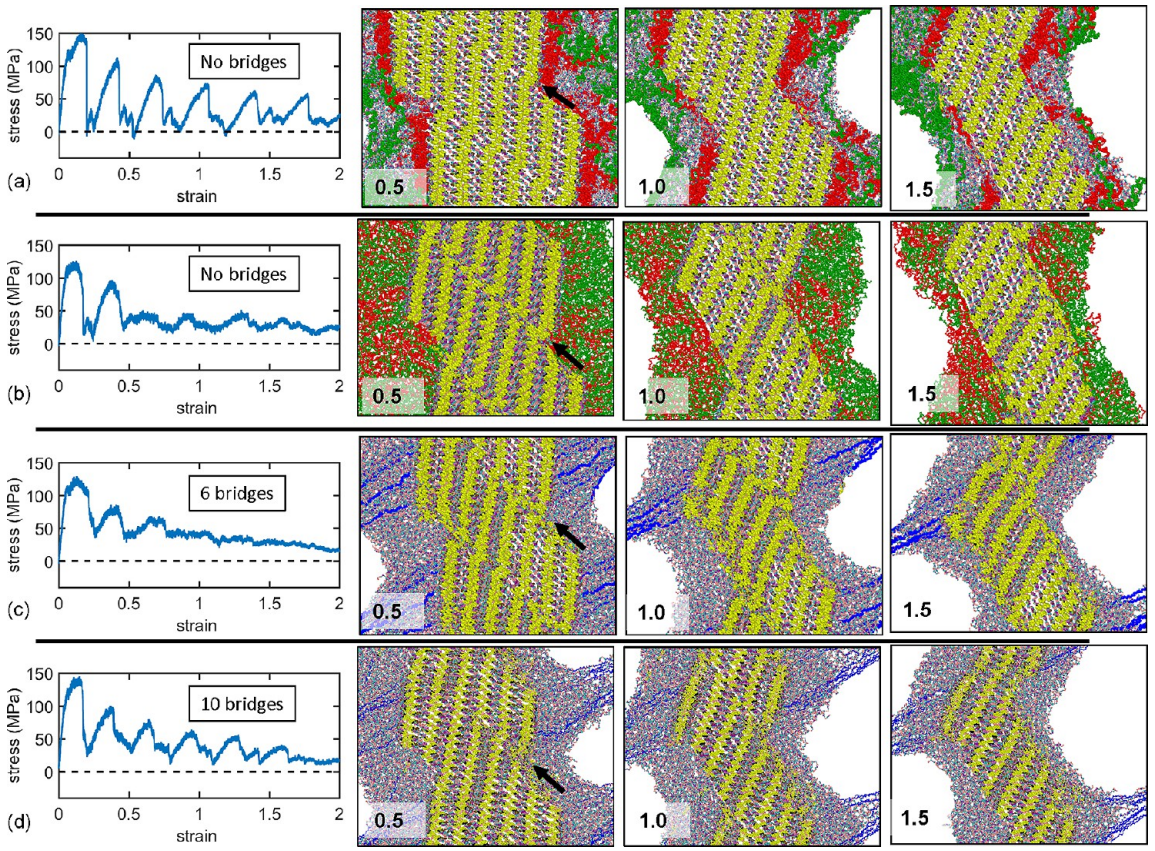


**Figure 7.** Engineering stress−strain curves and structural evolutions showing formation of shear bands in the hard domain during lateral tensile straining along the *z*-direction. The stress reported here is the normal stress component along the loading direction. Configuration 1: (a) same color code as in Figure 3; configuration 4: (b), configuration 8: (c) only bridges are colored blue. configuration 9: (d) only bridges are colored blue. The arrows in the configuration snapshots point to the locations of shear bands. Strain values are labeled. The structure is represented using periodic images of the simulation cell replicated along the *z*-direction, and the entire system has been translated along the *x*-direction to put the hard domain at the center of the image. It is found that wide shear bands are associated with less prominent sawtooth features in the stress−strain curves and that the bridging constraints mitigate the stress relaxation by pulling on the hard domain.

containing bridges and not containing loop−loop bridging entanglements (e.g., configuration 6, Figure 5c), the strength is approximately linearly proportional to the number of bridges (see also Figure S8). This linearly scaling of strength can be traced approximately to the number of hard segments being loaded at once. The resistance to pull-out should be about the same for each hard segment (we estimate a value of about 0.4 nN per hard segment; cf. Figure S8) so that the total force becomes linearly proportional to the number of hard segments connected by bridges as those bridges are pulled taut.

The linear scaling described above also applies to loop−loop bridging entanglements based on a similar physical understanding (Figure S8). Unlike bridges, however, a single loop−loop bridging entanglement may exhibit a "pulley-like" motion (Figure S9), through which about equal force is applied to four hard segments when the loops are stretched, rather than only two as is the case for a single stretched bridge. Because of the "pulley" effect, there may be slight difference in structure evolution during strain. For example, in the case of configuration 11 (Figure 5f,g and Figure S9), one hard segment is completely pulled out, while three hard segments are only partially pulled out. The difference is that if we compare a single loop−loop bridging entanglement with two bridges (since they have the same number of connected hard segments) under a significantly large tensile deformation, a single loop−loop bridging entanglement can be relaxed by pulling out just one of the four hard segments, whereas a system containing two bridges must pull out two hard segments, one for each bridge. On a side note, pulleys made from polymer chains can be found in experiments.[37]

Figure 6 illustrates the mechanism of deformation when strained along the *y*-direction lateral to the lamellar stack. In this deformation mode, after the first yield event (cavitation), the disentanglement and chain pull-out typical of strain in the *x*-direction are superseded by melting of the hard domain in the form of shear bands of finite width. This shear band formation is insensitive to interface topology. The melting behavior in the hard domain is caused by shear stress (Figure 6c). Within each shear band, hydrogen bonds are broken and re-formed in a disorganized fashion, resulting in disordering of the MDI/BDO hard segments within the shear bands and the appearance of localized "melting". Shear band formation is preceded by some breaking and re-forming of hydrogen bonds within the hard domain, but around 20% strain the disordering becomes localized into distinct shear bands. Once formed, these shear bands provide a "soft" mechanism for continued plastic deformation.

Figure 7 illustrates the mechanism of deformation when strained along the *z*-direction, lateral to the lamellar stack. Similar to the *y*-direction response, the second yield event is associated with shearing of the hard domain. However, in this case, the width of the shear band varies. Both wide and narrow


DOI: 10.1021/acs.macromol.7b02367
*Macromolecules* XXXX, XXX, XXX−XXX

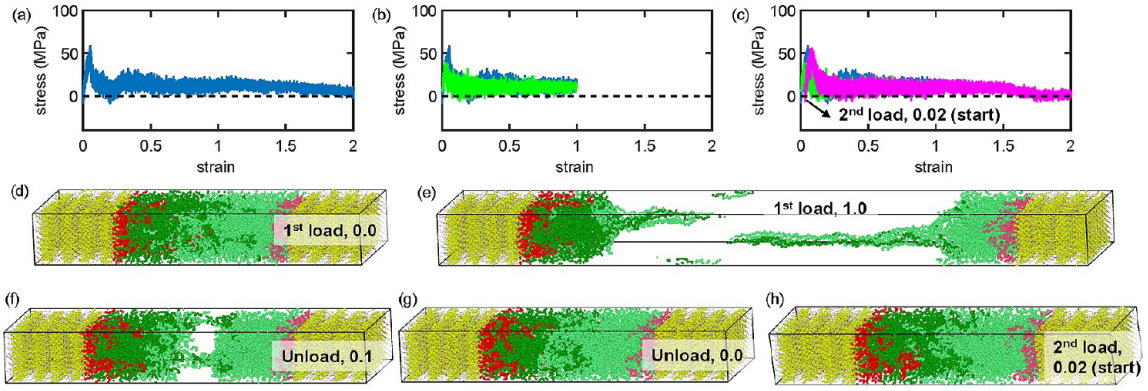


**Figure 8.** Engineering stress−strain curves and structural evolutions of configuration 1 ("no bridges") during cyclic tensile straining along the *x*-direction. The stress reported here is the normal stress component along the loading direction. (a) First loading stress−strain curve. (b) Unloading stress−strain curve (green) from 100% strain, overlapping the first loading stress−strain curve. (c) Second loading stress−strain curve (purple). In structural evolutions images, loops and tails originated from the left hard domain surface are colored red and dark green, while loops and tails originated from the right hard domain surface are colored pink and light green. Strain values and the orders of loading are labeled on structural evolution images. No significant Mullins effect is observed, but rather viscoelastic sliding and rearrangement of soft segments.

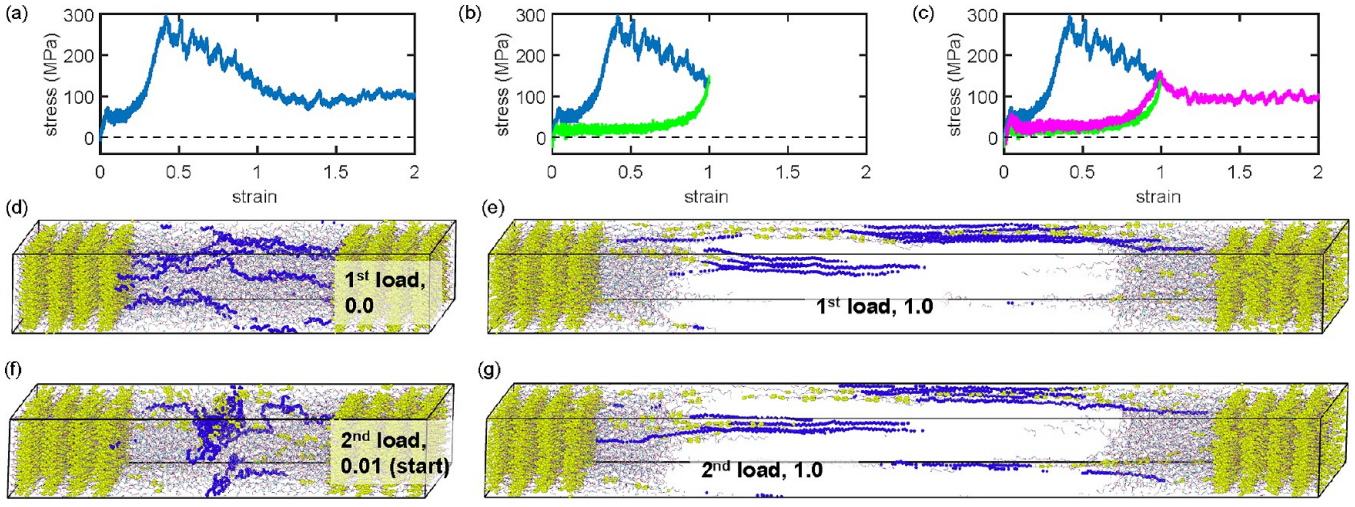


**Figure 9.** Engineering stress−strain curves and structural evolution of configuration 8 (from the "with bridges" subensemble) during cyclic tensile deformation along the *x*-direction. The stress reported here is the normal stress component along the loading direction. (a) First loading stress−strain curve. (b) Unloading stress−strain curve (green) from 100% strain, overlapping on the first loading stress−strain curve. (c) Second loading stress−strain curve (purple). Similar to the case of configuration 1 (from the "no bridges" subensemble), we find that the length along the loading direction of the equilibrated structure after one cycle of deformation is slightly longer than that of its initial, undeformed structure, corresponding to a residual strain around 1% (f). Bridges are highlighted in blue and aromatic carbon rings in the hard domain are highlighted in yellow. Strain values and cycle numbers are labeled on the configuration snapshots. A significant Mullins effect is observed due to the pulling out of hard segments, which is not recoverable during unloading, and thus huge energy is dissipated.

shear bands are observed, regardless of topological subensemble. The relatively narrow shear bands of Figures 7a and 7d are indicative of block slip, which manifests as sawtooth features on the corresponding stress−strain curves and the high yield stress during each yield cycle. The relatively wide shear bands of Figures 7b and 7c involve some degree of local disordering within the shear band, similar to the *y*-direction response, resulting in a softer, less cyclic stress−strain response. Therefore, the width of the shear band is directly related to the stress relaxation. Unlike straining along the *y*-direction (Figure 6), the formation of shear bands is not preceded by disordering in the hard domain associated with breaking and re-forming of hydrogen bonds. As mentioned before, the straining along the *z*-direction does not directly stretch the hydrogen bonding plane. Therefore, the essence of block slip is the highly concerted motion of planes of hard segments linked by hydrogen bonds, and the major resistance to slip is due to steric interactions between these planes. Another observation is that regardless of the width of the shear band, the "with bridges" subensemble usually exhibits less stress relaxation when strained along the *z*-direction when compared to the "no bridges" subensemble. Such observation is directly correlated to the constraining effect from bridging topology in the interphase, as explained earlier.

**3.3. Behavior under Cyclic Tensile Deformation.** Next, we examine the behavior of the TPU under cyclic loading. Such simulations offer insight into the molecular origins of recovery, toughening, and the Mullins effect. Figure 8 illustrates the stress−strain curves and structural evolution of configuration 1 during cyclic tensile deformation along the *x*-direction. Figure 8a shows the stress−strain response up to 200% strain (same as Figure 3a). Figure 8b shows the stress recovery upon reversal of


DOI: 10.1021/acs.macromol.7b02367
*Macromolecules* XXXX, XXX, XXX−XXX

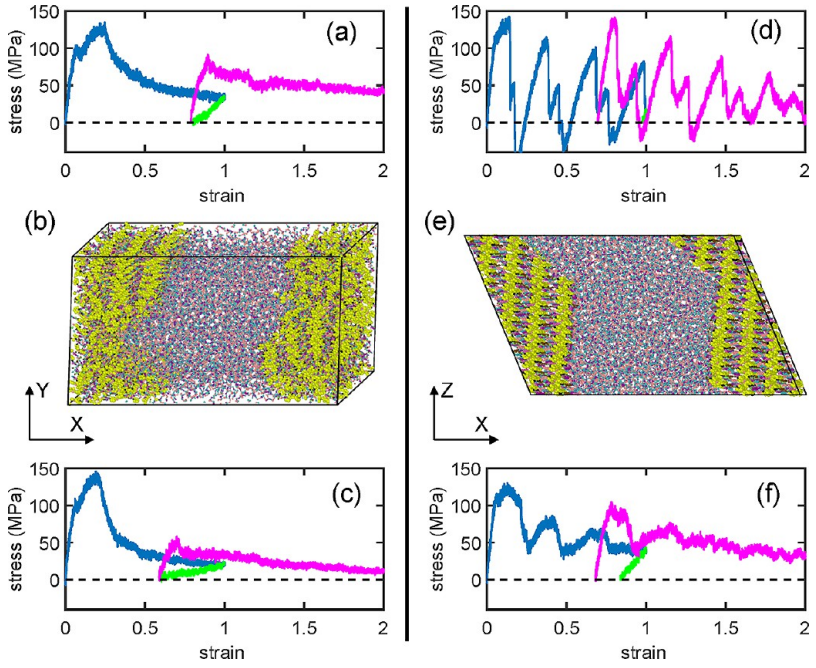


**Figure 10.** Stress−strain curves during cyclic tensile straining along the lateral directions. The stress reported here is the normal stress component along the loading direction. The first loading curve is shown in blue. The unloading curve is shown in green. The second loading curve is shown in purple. (a) The engineering stress−strain curve of configuration 2 (from the "no bridges" subensemble) during cyclic tensile straining along the *y*-direction. (b) The equilibrated structure of configuration 2 before the second loading (the starting configuration for the purple curve in (a)). (c) The engineering stress−strain curve of configuration 9 (from the "with bridges" subensemble) during cyclic tensile straining along the *y*-direction. (d) The engineering stress−strain curve of configuration 3 (from the "no bridges" subensemble) during cyclic tensile straining along the *z*-direction. (e) The equilibrated structure of configuration 3 before the second loading (the starting configuration for the purple curve in (d)). (f) The engineering stress−strain curve of configuration 8 (from the "with bridges" subensemble) during cyclic tensile straining along the *z*-direction. It is found that when loading laterally, the more degradation of crystallinity in the hard domain, the stronger the Mullins effect.

strain starting at 100% strain. Remarkably, the deformation appears to be almost completely reversible: the stress first starts to increase near 20% strain, peaks near the same stress and strain as the first yield event, and then drops toward zero. This behavior is indicative of closing of the cavity (Figures 8f to 8g) and healing of the interface within the soft domain.

We then re-equilibrated the structure in Figure 8g for 2 ns and observed a residual strain of only 2% (Figure 8h) relative to the *x*-dimension of the simulation cell before the first straining (Figure 8c). This is the consequence of the disentanglement of tails and loops during the first leg of tensile deformation. Comparison of Figure 8d (before first straining) to Figure 8g (after first complete strain cycle) shows that tails originating from the left interface (dark green) and the right interface (light green) are less well-mixed after one cycle of tensile deformation. In general, such demixing of soft segments incurs both entropic and enthalpic costs. This demixing is the origin of the residual 2% strain after re-equilibration.

Finally, we examine the response of configuration 1 (Figure 8, "no bridges") to a second leg of tensile deformation. As in the first cycle, the first yield event is due to cavitation. However, the second yield event, which appears in the first tensile deformation leg around 30% strain, is absent from the second tensile deformation leg. Furthermore, the stress level during reloading is only slightly lower than the first loading (Figure S10). Such a slight softening of mechanical response is typical of viscoelastic material behavior. According to our interpretation of Figure 3a, the second yield event is due to the stretching and disentangling of tails and loops; as a result of strain-induced topological demixing, some of these entanglements are eliminated by deformation, so that little or no second yield event is observed during the second deformation. In other words, some of the work performed during the first loading was completely dissipated, which is the molecular mechanism of the observed viscoelastic behavior. In effect, such elimination of entanglements during the first loading gives rise to the earlier onset of complete disentanglement in the second loading, as indicated by zero stress around 175% strain.

Figure 9 shows the stress−strain curves and structural evolution of configuration 8 during cyclic tensile straining along the *x*-direction, typical of the "with bridges" subensemble. Here, instead of a typical viscoelastic behavior, we see a prominent Mullins effect. The unloading starts at 100% strain (Figure 9b). Strikingly, the stress−strain curve upon second loading shows a much softer mechanical response compared to that from the first loading. In addition, the stress−strain curve from the second loading almost overlaps that from first loading beyond the maximum strain of the first loading cycle (i.e., 100% strain). The mechanism can be readily deciphered from the configuration snapshots. From the understanding established earlier, the stretching of bridges causes the initial increase in stress, followed by the ensuing pull-out of hard segments from the hard domain, which is responsible for the second yield event. The salient sawtooth features in the stress−strain curve after the second yield event are the signature of successive pulling out of hard segments. However, once pulled out, the hard segments are not restored upon unloading to their original place within the hard domain. Therefore, a huge amount of energy is dissipated irreversibly during the first cycle of loading and unloading. In general, the pulled-out hard segments and


DOI: 10.1021/acs.macromol.7b02367
*Macromolecules* XXXX, XXX, XXX−XXX

the connected bridges simply collapse back into high-energy conformations in the soft domain for a time that is long compared to the duration of our simulations. Thus, upon second loading, these conformations unfold more easily up to the maximum strain of the previous cycles (Figure 9g), without the need to repeat the processes of the previous loading cycles. The resulting hysteresis is indicative of the Mullins effect.

Figure 10 illustrates the stress−strain curves of several configurations during cyclic tensile straining along the lateral directions. Configurations were drawn from both topological subensembles ("with bridges" and "no bridges"). Figure 10a shows the engineering stress−strain curve of configuration 2 during cyclic tensile straining along the *y*-direction. The unloading starts at 100% strain. One can see that the shear band region in the hard domain does not recrystallize (Figure 10b), and the major portion of the elongation during first loading is not reversed during unloading. Upon unloading, we re-equilibrate the structure before the second loading. During the equilibration, the cavity in the soft domain (e.g., those in Figure 3b) again closes (Figure 10b). The second loading gives a smaller yield stress, indicating a softened mechanical response. Evidently, localized melting of the hard domain is responsible for the decrease in strength. Similar stress−strain behavior can be seen in Figure 10c, which shows the stress−strain curve of configuration 9 (from the "with bridges" subensemble) during cyclic deformation along the *y*-direction. Figure 10d shows the stress−strain curve of configuration 3 during cyclic deformation along the *z*-direction. The unloading starts at 100% strain. One can see that block slip in the hard domain is not reversed upon unloading (Figure 10e). During the equilibration before the second loading, the cavity in the soft domain (e.g., those in Figure 3c) again closes (Figure 10e), as was also the case in Figures 8 and 9; one concludes that cavitation, while important in yield, is reversible in general upon unloading and therefore not the source of hysteresis. The second loading gives quite similar yield stress. The sawtooth feature exhibited during the second loading stress−strain curve indicates the repeated process of block slip with a very narrow width of shear band (e.g., Figure 7a). In such case, we do not see much softening of mechanical response during the second loading. In general, we conclude that the narrower the width of shear band, the less the degradation of crystallinity in the hard domain as a result of block slip and therefore the less the softening in mechanical response. Nevertheless, for shear bands of finite width (e.g., configuration 8, Figure 7c), the second loading gives a smaller yield stress (Figure 10f), which is indicative of softening. Evidently, the molecular origin of the Mullins effect for lateral loading lies in the existence of a finite width of localized melting of the hard domain within the shear band.

## 4. CONCLUDING REMARKS

In this study, we report molecular mechanisms operative during large tensile deformation of a common type of thermoplastic polyurethane using molecular dynamics simulations. Deformations were performed at constant strain rate, up to engineering strains of 200% in tension. The TPU model was constructed using the Interphase Monte Carlo (IMC) method, so that both the chemical connectivity and the molecular packing of hard and soft segments within their respective domains, as well as between domains, are respected. Detailed examination of the evolution of structure with deformation was used to interpret the molecular mechanisms underlying the observed features of the stress−strain response. We present the large deformation mechanisms in the context of two topological subensembles, three orthogonal loading directions (*x*, *y*, and *z*), and cyclic loading.

Through a detailed examination of the structural changes accompanying large strain tensile deformation, a rich variety of molecular scale mechanisms are revealed within this TPU, some of which are recoverable and others that are not. In tension, these mechanisms include cavitation and disengagement of tail−tail and tail−loop entanglements within the soft domain as well as a gradual destruction of the hard domain through a combination of pulling out of hard segments, block slip, shear band formation, and localized melting. The resilience of TPUs is mainly enabled by the existence of bridges. These bridges are stretched in tension, and entropic elasticity plays an important role.

To facilitate the discussion, we posed six questions to be addressed by a detailed analysis of the configurations in each ensemble and for each mode of deformation. Here, we summarize our answers to those questions as follows. (1) The direction-dependent response is related to how the loads are distributed among soft and hard component for different loading directions (i.e., loading along stack direction is analogous to loading springs with different stiffnesses in series) and the orientation of hydrogen bonding plane. (2) Cavitation in the soft domain causes the initial yielding when strained in the stack direction. (3) Hard segments can be pulled out in the "with bridges" subensemble, when strained in the stack direction. The pulling-out process stretches both soft and hard components, significantly increasing the stress level. (4) Straining laterally and in parallel with the hydrogen bonding plane, shear band formation and localized melting of the hard domain occur. (5) Straining laterally and perpendicular to the hydrogen bonding plane, block slip occurs within the hard domain. (6) The presence of bridges helps to mitigate the stress relaxation during block slip in the hard domain.

From the simulations of cyclic loading, it is found that the most prominent mechanism for energy dissipation, or toughening, is related to destruction of the hard domain, in the forms of pulling out of hard segments, block slip, shear band formation, and localized melting. Since hydrogen bonding is important for the hard domain to maintain its crystal phase, it is expected that the pulling out of hard segments, shear band formation, and melting are closely related to the breaking and re-forming of hydrogen bonds. In this scenario, the release of hydrogen bonding energy is the physical source of energy dissipated. Block slip occurs predominantly between planes of hydrogen-bonded hard segments, is resisted only by steric interactions, and usually does not require deformation of the hydrogen bonding planes themselves. In block slip, the energy to overcome the steric interaction is completely dissipated. In line with the toughening mechanism, the breakdown of the hard domain is largely responsible for the Mullins effect and is typically irreversible. The energy has been dissipated during the structural change so that upon reloading less energy is needed to cover the loading path up to the unloading point, and therefore a softening of mechanical response is observed.

A number of important questions remain. For example, one can wonder whether the same mechanisms observed tension are also manifested in compression or other modes of deformation. Second, some mechanisms are likely to be precluded by the size of the lamellar stack model employed here. A complete description of the mechanical response of the


DOI: 10.1021/acs.macromol.7b02367
*Macromolecules* XXXX, XXX, XXX−XXX

complex heterogeneous TPU morphology would require, at a minimum, a multiscale model that includes a distribution of lamellar stacks in various orientations, as illustrated in Figure 1a. With increasing aspect ratio of the layers, it may become possible to observe buckling instabilities[38] under some conditions due to lateral compressive forces exerted on the layers as a result of Poisson effects, for example. However, the large lateral dimensions required for such mechanisms to become important would be very compute-intensive. Third, it is acknowledged that many mechanical responses are strongly dependent upon strain rate. In the preceding work by Lempesis et al., even the elastic constants for TPUs were found to be strain rate dependent.[26] Significantly lower strain rates, however, remain beyond the reach of current atomistic simulations.

The findings reported here accord qualitatively with several experimental observations reported in the literature for similarly heterogeneous polymeric systems, while the atomistic resolution offers further insights into the molecular mechanisms involved. For example, the microstructural breakdown in the hard domain is expected to occur in polyureas as well and would contribute to softening and the related hysteretic behaviors observed there.[18] In addition, the mixing of hard and soft segments at the interface due to chain pull-out and block slip revealed in this study would manifest as a gradual change in the electron density gradient associated with a "fuzzy interface".[19] Furthermore, the same structural changes in the hard domain would contribute to a decreased density of physical cross-links between polymer chains and a drop in the effective volume fraction of hard domains.[19] Finally, in a third experimental study where a TPU cross-linked by functionalized silica was subjected to large tensile deformation up to 200% engineering strain,[39] analysis of the nanostructure evolution led the authors to conclude that chain pull-out was responsible for dissociation of a previously unimodal ensemble of microfibrils and formation of a new ensemble of scattering entities; such a mechanism was observed directly in the current study. The molecular mechanisms extracted from our simulations thus serve to confirm certain hypotheses for the mechanistic interpretation of large strain deformation of heterogeneous polymeric systems, while revealing other, perhaps equally important, mechanisms. We hope such revelations may prove useful for future multiscale approaches to modeling the complex but vitally important mechanical behaviors of multiphase heterogeneous polymers containing mechanically distinct domains.

## ■ ASSOCIATED CONTENT

### Supporting Information

The Supporting Information is available free of charge on the ACS Publications website at DOI: 10.1021/acs.macromol.7b02367.

(1) Estimation of hydrogen bonding strength; (2) simulation model construction; (3) ensemble-averaged stress−strain curves showing other normal stress components; and (4) supplementary structure evolution data (PDF)

## ■ AUTHOR INFORMATION

### Corresponding Author

*E-mail rutledge@mit.edu (G.C.R.).

### ORCID

Nikolaos Lempesis: 0000-0002-4104-9666
Gregory C. Rutledge: 0000-0001-8137-1732

### Notes

The authors declare no competing financial interest.

## ■ ACKNOWLEDGMENTS

We gratefully acknowledge BASF SE for financial support.

## ■ REFERENCES

(1) Zia, K.; Bhatti, H.; Bhatti, I. Methods for polyurethane and polyurethane composites, recycling and recovery: A review. *React. Funct. Polym.* **2007**, *67* (8), 675−692.
(2) Zdrahala, R.; Zdrahala, I. Biomedical applications of polyurethanes: A review of past promises, present realities, and a vibrant future. *J. Biomater. Appl.* **1999**, *14* (1), 67−90.
(3) Wu, J.; Wang, N.; Wang, L.; Dong, H.; Zhao, Y.; Jiang, L. Unidirectional water-penetration composite fibrous film via electrospinning. *Soft Matter* **2012**, *8* (22), 5996−5999.
(4) Yang, Y.; Chen, Y.; Wei, Y.; Li, Y. 3D printing of shape memory polymer for functional part fabrication. *International Journal of Advanced Manufacturing Technology* **2016**, *84* (9−12), 2079−2095.
(5) McBane, J.; Sharifpoor, S.; Cai, K.; Labow, R.; Santerre, J. Biodegradation and in vivo biocompatibility of a degradable, polar/hydrophobic/ionic polyurethane for tissue engineering applications. *Biomaterials* **2011**, *32* (26), 6034−6044.
(6) Gu, X.; Mather, P. Water-triggered shape memory of multiblock thermoplastic polyurethanes (TPUs). *RSC Adv.* **2013**, *3* (36), 15783−15791.
(7) Koh, E.; Lee, S.; Shin, J.; Kim, Y. Renewable Polyurethane Microcapsules with Isosorbide Derivatives for Self-Healing Anticorrosion Coatings. *Ind. Eng. Chem. Res.* **2013**, *52* (44), 15541−15548.
(8) Yang, S.; Wang, L.; Wang, C.; Chen, L.; Chen, S. Superhydrophobic Thermoplastic Polyurethane Films with Transparent/Fluorescent Performance. *Langmuir* **2010**, *26* (23), 18454−18458.
(9) Wu, N.; Jing, B.; Cao, Q.; Wang, X.; Kuang, H.; Wang, Q. A novel electrospun TPU/PVdF porous fibrous polymer electrolyte for lithium ion batteries. *J. Appl. Polym. Sci.* **2012**, *125* (4), 2556−2563.
(10) Lempesis, N.; in 't Veld, P. J.; Rutledge, G. C. Simulation of the structure and mechanics of crystalline 4,4 '-diphenylmethane diisocyanate (MDI) with n-butanediol (BDO) as chain extender. *Polymer* **2016**, *107*, 233−239.
(11) Lempesis, N.; in 't Veld, P. J.; Rutledge, G. C. Atomistic Simulation of the Structure and Mechanics of a Semicrystalline Polyether. *Macromolecules* **2016**, *49* (15), 5714−5726.
(12) Sarva, S.; Deschanel, S.; Boyce, M. C.; Chen, W. Stress-strain behavior of a polyurea and a polyurethane from low to high strain rates. *Polymer* **2007**, *48* (8), 2208−2213.
(13) Yi, J.; Boyce, M. C.; Lee, G.; Balizer, E. Large deformation rate-dependent stress-strain behavior of polyurea and polyurethanes. *Polymer* **2006**, *47* (1), 319−329.
(14) Cho, H.; Rinaldi, R.; Boyce, M. C. Constitutive modeling of the rate-dependent resilient and dissipative large deformation behavior of a segmented copolymer polyurea. *Soft Matter* **2013**, *9* (27), 6319−6330.
(15) Cho, H.; Bartyczak, S.; Mock, W.; Boyce, M. C. Dissipation and resilience of elastomeric segmented copolymers under extreme strain rates. *Polymer* **2013**, *54* (21), 5952−5964.
(16) Qi, H.; Boyce, M. C. Stress-strain behavior of thermoplastic polyurethanes. *Mech. Mater.* **2005**, *37* (8), 817−839.
(17) Cho, H.; Mayer, S.; Poeselt, E.; Susoff, M.; in't Veld, P. J.; Rutledge, G. C.; Boyce, M. C. Deformation mechanisms of thermoplastic elastomers: Stress-strain behavior and constitutive modeling. *Polymer* **2017**, *128*, 87−99.
(18) Rinaldi, R.; Boyce, M. C.; Weigand, S.; Londono, D.; Guise, M. Microstructure Evolution during Tensile Loading Histories of a Polyurea. *J. Polym. Sci., Part B: Polym. Phys.* **2011**, *49* (23), 1660−1671.


DOI: 10.1021/acs.macromol.7b02367
*Macromolecules* XXXX, XXX, XXX−XXX

(19) Sui, T.; Salvati, E.; Ying, S.; Sun, G.; Dolbnya, I. P.; Dragnevski, K.; Prisacariu, C.; Korsunsky, A. M. Strain softening of nano-scale fuzzy interfaces causes Mullins effect in thermoplastic polyurethane. *Sci. Rep.* **2017**, *7*, 916.
(20) Balijepalli, S.; Rutledge, G. C. Molecular simulation of the intercrystalline phase of chain molecules. *J. Chem. Phys.* **1998**, *109* (16), 6523−6526.
(21) Gautam, S.; Balijepalli, S.; Rutledge, G. C. Molecular simulations of the interlamellar phase in polymers: Effect of chain tilt. *Macromolecules* **2000**, *33* (24), 9136−9145.
(22) in't Veld, P. J.; Rutledge, G. C. Temperature-dependent elasticity of a semicrystalline interphase composed of freely rotating chains. *Macromolecules* **2003**, *36* (19), 7358−7365.
(23) in 't Veld, P. J.; Hütter, M.; Rutledge, G. C. Temperature-dependent thermal and elastic properties of the interlamellar phase of semicrystalline polyethylene by molecular simulation. *Macromolecules* **2006**, *39* (1), 439−447.
(24) Lee, S.; Rutledge, G. C. Plastic Deformation of Semicrystalline Polyethylene by Molecular Simulation. *Macromolecules* **2011**, *44* (8), 3096−3108.
(25) Kim, J.; Locker, C. R.; Rutledge, G. C. Plastic Deformation of Semicrystalline Polyethylene under Extension, Compression, and Shear Using Molecular Dynamics Simulation. *Macromolecules* **2014**, *47* (7), 2515−2528.
(26) Lempesis, N.; in 't Veld, P. J.; Rutledge, G. C. Atomistic Simulation of a Thermoplastic Polyurethane and Micromechanical Modeling. *Macromolecules* **2017**, *50* (18), 7399−7409.
(27) Feyereisen, M.; Feller, D.; Dixon, D. Hydrogen bond energy of the water dimer. *J. Phys. Chem.* **1996**, *100* (8), 2993−2997.
(28) Wendler, K.; Thar, J.; Zahn, S.; Kirchner, B. Estimating the Hydrogen Bond Energy. *J. Phys. Chem. A* **2010**, *114* (35), 9529−9536.
(29) Fernández-d'Arlas, B.; Rueda, L.; Fernández, R.; Khan, U.; Coleman, J. N.; Mondragon, I.; Eceiza, A. Inverting Polyurethanes Synthesis: Effects on Nano/Micro-Structure and Mechanical Properties. *Soft Mater.* **2010**, *9* (1), 79−93.
(30) McLean, R. S.; Sauer, B. B. Tapping-Mode AFM Studies Using Phase Detection for Resolution of Nanophases in Segmented Polyurethanes and Other Block Copolymers. *Macromolecules* **1997**, *30* (26), 8314−8317.
(31) Furukawa, M.; Kojio, K.; Kugumiya, S.; Uchiba, Y.; Mitsui, Y. Microphase Separation of Bulk and Ultrathin Films of Polyurethane Elastomers. *Macromol. Symp.* **2008**, *267* (1), 9−15.
(32) Aneja, A.; Wilkes, G. L. A systematic series of 'model' PTMO based segmented polyurethanes reinvestigated using atomic force microscopy. *Polymer* **2003**, *44* (23), 7221−7228.
(33) Choi, T.; Weksler, J.; Padsalgikar, A.; Runt, J. Influence of soft segment composition on phase-separated microstructure of polydimethylsiloxane-based segmented polyurethane copolymers. *Polymer* **2009**, *50* (10), 2320−2327.
(34) Garrett, J. T.; Siedlecki, C. A.; Runt, J. Microdomain morphology of poly (urethane urea) multiblock copolymers. *Macromolecules* **2001**, *34* (20), 7066−7070.
(35) Plimpton, S. Fast parallel algorithms for short-range molecular-dynamics. *J. Comput. Phys.* **1995**, *117* (1), 1−19.
(36) Irving, J.; Kirkwood, J. The statistical mechanical theory of transport processes 0.4. The equations of hydrodynamics. *J. Chem. Phys.* **1950**, *18* (6), 817−829.
(37) Choi, S.; Kwon, T.; Coskun, A.; Choi, J. Highly elastic binders integrating polyrotaxanes for silicon microparticle anodes in lithium ion batteries. *Science* **2017**, *357* (6348), 279.
(38) Makke, A.; Perez, M.; Lame, O.; Barrat, J. L. Nanoscale buckling deformation in layered copolymer materials. *Proc. Natl. Acad. Sci. U. S. A.* **2012**, *109* (3), 680−685.
(39) Stribeck, N.; Zeinolebadi, A.; Harpen, F.; Luinstra, G.; Eling, B.; Botta, S. Thermoplastic Polyurethane Cross-Linked by Functionalized Silica. Nanostructure Evolution under Mechanical Load. *Macromolecules* **2013**, *46* (10), 4041−4052.



DOI: 10.1021/acs.macromol.7b02367
*Macromolecules* XXXX, XXX, XXX−XXX